Soft Matter

PAPER

View Article Online
View Journal | View Issue

Cite this: *Soft Matter*, 2024, **20**, 5456

Plateau–Rayleigh instability of a soft layer coated on a rigid cylinder

Bharti, Andreas Carlson and Tak Shing Chan *

Received 16th January 2024,
Accepted 7th June 2024

DOI: 10.1039/d4sm00061g

rsc.li/soft-matter-journal

We study the Plateau–Rayleigh instability of a soft viscoelastic solid layer coated on a rigid cylinder *i.e.*, a soft fibre with a rigid core. The onset of instability is examined using a linear stability analysis. We find that increasing the rigid cylinder radius or the stiffness of the layer reduces the growth rate of the fastest growing mode. For each rigid cylinder radius, a critical elastocapillary number is found below which all wavelengths of disturbances are stable. The critical value for a soft fibre with a thick rigid cylindrical core can be several orders of magnitudes larger than that for a totally soft fibre (no rigid core). This highlights the strong stabilizing effect of the rigid core on the system. Increasing the relaxation timescale of the viscoelastic material also slows down the growth of disturbances, but has no effect on the critical elastocapillary number. Interestingly, the wavelength of the fastest growing mode is independent of the rigid cylinder radius for the purely elastic case.

1 Introduction

Significant stress is usually required for a solid to deform, and as such the effects due to surface tension have often been ignored. Soft solids such as elastomers and gels,[1] and biological materials such as protein condensates,[2] cells and tissues,[3] on the other hand, have elastic moduli ranging between kPa and MPa, which means that they can deform much easier. In recent years, there has been significant attention to how capillary effects can lead to soft solid deformations, and fascinating elastocapillary phenomena have been discovered.[4–8] The Plateau–Rayleigh instability (PRI),[9,10] namely the instability driven by surface tension and often illustrated by the breakup of liquid jets into droplets,[11] has currently been examined for fibres made of soft solids.[12–21]

Studies of the PRI of soft fibres have focused on soft materials that demonstrate elastic or viscoelastic responses.[12–21] An experimental study using soft agar gel fibres by Mora *et al.*[14] has shown that the instability occurs when the elastocapillary length $\gamma/\mu \geq 6R$, where R is the radius of the soft fibre, γ is the solid surface tension and μ is the shear modulus. Other studies of the PRI on a soft fibre include, for example, the formation of bead-on-string structures.[12,16,18,22] Another interesting factor that might significantly modify the instability is having an inner rigid core, *i.e.* a fibre consists of a soft-layer-coated on a rigid cylinder. Such a kind of setup, but with a coated liquid film instead of a soft solid layer, has been studied extensively[23–32] since the early works in the 1960s by Goren.[33,34] Recent studies on this problem have addressed the effects of liquid slip on the solid surface[28,32] and the dynamics of the droplets formed on the fibre.[25] However, investigations on situations in which the coated layer is a soft solid are still missing. How viscoelastic properties and the rigid core influence the PRI of a soft-layer-coated fibre remain unclear, which is addressed in this article.

Soft solids have recently been used in many applications, for example in 3D bioprinting,[35] mimicking muscle tissues in biomedicine[36] and water harvesting.[37] In living organisms, soft fibrous-shaped structures are often found in cellular tubes and compartments of cells. Instability of these biological ingredients have been rationalised through the PRI.[38–42] One example is a recent study on the undulation and droplet formation of a layer of condensed protein TPX2 on a microtubule.[42] Hence, investigating the PRI of fibrous soft solids is becoming more important for both understanding the fundamental physical problems and the development of new technologies. In this study, we examine the onset of PRI of a soft layer coated on a rigid cylinder through a linear stability analysis.

2 Formulation

We consider a rigid cylinder of radius r_0 coated with a layer of incompressible viscoelastic material of density ρ and uniform thickness H at an undeformed state. The whole fibre consisting of the rigid cylinder and the coated soft layer has a total radius $R = r_0 + H$ as shown in Fig. 1. Consider that the fiber is thin enough such that the Bond number $\mathrm{Bo} \equiv \rho g R^2/\gamma \ll 1$, where g is the gravitational acceleration, which allows us to neglect the effect of gravity. By only consider viscoelastic stresses, the equation of motion of a soft material element is

Mechanics Division, Department of Mathematics, University of Oslo, 0316 Oslo, Norway. E-mail: taksc@uio.no

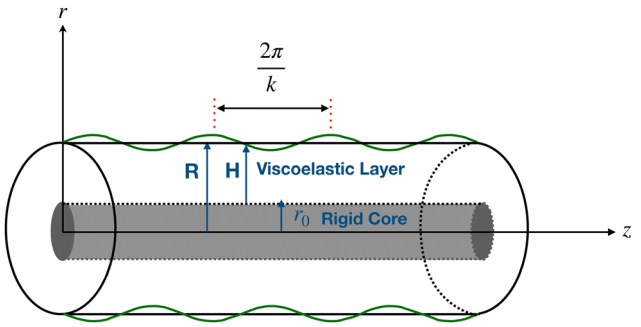

Fig. 1 Schematic representation of an infinitely long, rigid cylinder of radius r_0 coated with a layer of incompressible viscoelastic material of uniform thickness H at an undeformed state. A random disturbance of the interface of the viscoelastic layer is decomposed into sinusoidal deformations of wavenumber k. In cylindrical coordinate systems, r and z are respectively the radial coordinate and the longitudinal coordinate.

given by

$$\frac{\partial \sigma_{ij}(\boldsymbol{x},t)}{\partial x_j} = \rho \frac{\partial^2 u_i(\boldsymbol{x},t)}{\partial t^2} \tag{1}$$

where $\sigma_{ij}(\boldsymbol{x},t)$ and $u_i(\boldsymbol{x},t)$ are respectively the stress tensor and the displacement vector in index notation at a position vector $\boldsymbol{x}$ and time t. Assuming a linear viscoelastic response of the incompressible soft material, the relation between σ_{ij} and the strain tensor ε_{ij} is

$$\sigma_{ij}(\boldsymbol{x},t) = 2\int_{-\infty}^{t} \mu(t-t') \frac{\partial \varepsilon_{ij}(\boldsymbol{x},t')}{\partial t'} \mathrm{d}t' - p(\boldsymbol{x},t)\delta_{ij}, \tag{2}$$

where $\mu(t)$ is the shear relaxation function, p is the pressure, δ_{ij} is the Kronecker delta, and the strain tensor ε_{ij} is related to the displacement as

$$\varepsilon_{ij} = \frac{1}{2}\left(\frac{\partial u_i}{\partial x_j} + \frac{\partial u_j}{\partial x_i}\right). \tag{3}$$

There are different models that have been used to describe viscoelastic materials. The simplest models are the Kelvin–Voigt model or the Maxwell model, which consists of a spring and a viscous damper connected in parallel or in series respectively. In this study, we consider the soft material to behave as a gel described by the Chasset–Thirion model assuming a power law response given by

$$\mu(t) = \mu_o\left[1 + \Gamma(1-n)^{-1}\left(\frac{\tau}{t}\right)^n\right], \tag{4}$$

where μ_0 is the static shear modulus, τ is the relaxation timescale of the viscoelastic response, Γ is the gamma function and n is a parameter typically smaller than or equal to unity.

To compute the growth rate of disturbance on the viscoelastic layer, we follow the approach delineated by previous studies.[17,32] We decompose the time-dependent variables into normal modes e^{st}, where s is the growth rate. The amplitude of the normal mode of a function $f(t)$ is obtained by the Laplace transform defined as

$$\tilde{f}(s) = \int_0^\infty f(t)e^{-st}\mathrm{d}t. \tag{5}$$

We apply the Laplace transform to the constitutive relation (2) and obtain

$$\tilde{\sigma}_{ij}(\boldsymbol{x},s) = \hat{\mu}(s)\left[\frac{\partial \tilde{u}_i(\boldsymbol{x},s)}{\partial x_j} + \frac{\partial \tilde{u}_j(\boldsymbol{x},s)}{\partial x_i}\right] - \tilde{p}(\boldsymbol{x},s)\delta_{ij} \tag{6}$$

where $\tilde{\sigma}_{ij}$, $\tilde{u}_i$ and $\tilde{p}$ are respectively the Laplace transform of σ_{ij}, u_i and p, and $\hat{\mu}(s)$ is the shear modulus in Laplace space defined as

$$\hat{\mu}(s) \equiv s\int_0^\infty \mu(t)e^{-st}\mathrm{d}t = \mu_0[1 + (s\tau)^n]. \tag{7}$$

Thus the governing eqn (1) in Laplace space can be written as

$$\hat{\mu}(s)\frac{\partial^2 \tilde{u}_i}{\partial x_j \partial x_j} - \frac{\partial \tilde{p}}{\partial x_i} = \rho s^2 \tilde{u}_i. \tag{8}$$

Next, we scale the lengths with the radius of the whole fibre R, the time with the inertial-capillary time $t_c \equiv \sqrt{\rho R^3/\gamma}$ and the stresses by μ_o. We define the following dimensionless variables as

$$\bar{r} = \frac{r}{R},\ \bar{z} = \frac{z}{R},\ \bar{s} = t_c s, \tag{9}$$

$$\bar{u}_i(\bar{r},\bar{z},\bar{s}) = \frac{\tilde{u}_i}{t_c R}, \bar{p}(\bar{r},\bar{z},\bar{s}) = \frac{R\tilde{p}}{t_c\gamma}, \bar{\sigma}_{ij}(\bar{r},\bar{z},\bar{s}) = \frac{\tilde{\sigma}_{ij}}{t_c\mu_0}. \tag{10}$$

Note that variables in Laplace space have an additional dimension of time. The dimensionless form of the governing equation (eqn (8)) in Laplace space is

$$\frac{1}{\beta}\frac{\partial^2 \bar{u}_i}{\partial x_j \partial x_j} - \frac{\partial \bar{p}}{\partial x_i} = \bar{s}^2 \bar{u}_i \tag{11}$$

where

$$\beta \equiv \frac{\sum}{1 + (\bar{\tau}\bar{s})^n} \tag{12}$$

is the inverse of the dimensionless shear modulus in Laplace space which is a function of $\bar{s}$ and consists of 2 parameters: $\Sigma \equiv \gamma/(\mu_0 R)$ and $\bar{\tau} \equiv \tau/t_c$. In general, the expression of β depends on the viscoelastic model. The parameter Σ is called the elastocapillary number which compares the capillary pressure to the elastic stress. When $\Sigma \to \infty$, capillarity dominates over elasticity. The other parameter $\bar{\tau}$ is the ratio of the viscoelastic relaxation timescale to the inertial-capillary time and can be interpreted as the Deborah number since the material responds purely elastically when $\bar{\tau} = 0$. When $\bar{\tau} \to \infty$, viscoelastic effects are expected to dominate over inertial effects. To sum up, the dimensionless control parameters of the system are: $\bar{r}_0$, Σ, $\bar{\tau}$ and n.

We consider only the longitudinal disturbance and neglect the azimuthal disturbance as azimuthal normal modes always increase the surface energy.[11] The deformation of the soft layer is axisymmetric. We hence use the cylindrical coordinate system (r,ϕ,z) and the corresponding unit vectors are denoted

as $(\hat{r},\hat{\phi},\hat{z})$. The displacement vector is denoted as $u(r,z,t) = u_r(r,z,t)\hat{r} + u_z(r,z,t)\hat{z}$. Note that $u_\phi = 0$ due to axisymmetry.

The governing eqn (11) can be solved by applying the Helmholtz decomposition of the displacement as described in ref. 17 and 32. The general solutions are given as

$$\bar{p}(\bar{s}) = -\bar{s}^2[A_1 I_0(\bar{k}\bar{r}) + A_3 K_0(\bar{k}\bar{r})]e^{i\bar{k}\bar{z}}, \tag{13}$$

$$\bar{u}_r = [A_1\bar{k}I_1(\bar{k}\bar{r}) - A_2(i\bar{k})I_1(\alpha\bar{r}) - A_3\bar{k}K_1(\bar{k}\bar{r}) - A_4(i\bar{k})K_1(\alpha\bar{r})]e^{i\bar{k}\bar{z}}, \tag{14}$$

and

$$\bar{u}_z = [A_1(i\bar{k})I_0(\bar{k}\bar{r}) + A_2\alpha I_0(\alpha\bar{r}) + A_3(i\bar{k})K_0(\bar{k}\bar{r}) - A_4\alpha K_0(\alpha\bar{r})]e^{i\bar{k}\bar{z}} \tag{15}$$

where $\bar{k} \equiv kR$ is the dimensionless wavenumber, I and K are respectively the modified Bessel functions of the first and second kind, $\alpha = \sqrt{\bar{s}^2\beta + \bar{k}^2}$ is a function of $\bar{s}$ and $\bar{k}$, and is introduced here to simplify the expressions of equations, and $A_m (m = 1,2,3,4)$ are the undermined coefficients.

Next we impose the boundary conditions. At $\bar{r} = \bar{r}_0 \equiv r_0/R$, there is no penetration of material, thus

$$\bar{u}_r|_{\bar{r}=\bar{r}_0} = 0. \tag{16}$$

For the z-direction, we impose a no-slip condition

$$\bar{u}_z|_{\bar{r}=\bar{r}_0} = 0. \tag{17}$$

At $\bar{r} = 1$, we assume the slope of the deformed interface to be small. Balancing the Laplace pressure due to solid surface tension and the viscoelastic stresses gives

$$\bar{\sigma}_{rr}|_{\bar{r}=1} = \sum \left(\frac{\partial^2 \bar{u}_r}{\partial \bar{z}^2} + \bar{u}_r\right)\Bigg|_{\bar{r}=1}, \tag{18}$$

in the r-direction, and gives the vanishing shear stress

$$\bar{\sigma}_{rz}|_{\bar{r}=1} = 0 \tag{19}$$

in the z-direction.

3 Dispersion relation

Using the expressions of the general solutions (eqn (13)–(15)) for the boundary conditions (eqn (16)–(19)) yields a set of linear equations for the unknowns A_m which is given in Appendix 6.1. The solvability condition for non-trivial solutions of the linear equations with unknowns A_m is that the determinant is vanishing, which gives the following dispersion relation

$$\begin{vmatrix} \bar{k}I_1(\bar{r}_0\bar{k}) & -i\bar{k}I_1(\bar{r}_0\alpha) & -\bar{k}K_1(\bar{r}_0\bar{k}) & -i\bar{k}K_1(\bar{r}_0\alpha) \\ (i\bar{k})I_0(\bar{r}_0\bar{k}) & \alpha I_0(\bar{r}_0\alpha) & (i\bar{k})K_0(\bar{r}_0\bar{k}) & -\alpha K_0(\bar{r}_0\alpha) \\ C_1 & C_2 & C_3 & C_4 \\ 2i\bar{k}^2 I_1(\bar{k}) & (\bar{k}^2+\alpha^2)I_1(\alpha) & -2i\bar{k}^2 K_1(\bar{k}) & (\bar{k}^2+\alpha^2)K_1(\alpha) \end{vmatrix} = 0, \tag{20}$$

where

$$C_1 = \frac{\alpha^2+\bar{k}^2}{2}I_0(\bar{k}) - \bar{k}I_1(\bar{k}) - \frac{\beta}{2}(1-\bar{k}^2)\bar{k}I_1(\bar{k}),$$

$$C_2 = -i\bar{k}[\alpha I_0(\alpha) - I_1(\alpha)] + \frac{\beta}{2}i\bar{k}(1-\bar{k}^2)I_1(\alpha),$$

$$C_3 = \frac{\alpha^2+\bar{k}^2}{2}K_0(\bar{k}) + \bar{k}K_1(\bar{k}) + \frac{\beta}{2}(1-\bar{k}^2)\bar{k}K_1(\bar{k}),$$

$$C_4 = i\bar{k}[\alpha K_0(\alpha) + K_1(\alpha)] + \frac{\beta}{2}i\bar{k}(1-\bar{k}^2)K_1(\alpha).$$

when $\bar{r}_0 \to 0$, the modified Bessel functions $I_0(\bar{r}_0)$ and $I_1(\bar{r}_0)$ are bounded, but $K_0(\bar{r}_0)$ and $K_1(\bar{r}_0)$ diverge. These unbounded terms are eliminated for the case of $\bar{r}_0 = 0$.[17] To examine the feature of the dispersion relation for small $\bar{r}_0$, we expand the determinant of the dispersion relation (20) in series of $\bar{r}_0$. The result for the leading order terms is given in Appendix 6.2 which consists of logarithmic terms of $\bar{r}_0$.

4 Results

The validation of the dispersion relation (eqn (20)) is presented in Appendix 6.3 in which we compare our results in the Newtonian fluid limit with previous studies in the literature. In this section, we first consider the purely elastic solid limit and then we focus on the effects of viscoelasticity.

4.1 Purely elastic solid limit

When the viscoelastic relaxation timescale τ is small compared to the inertial-capillary time $\sqrt{\rho R^3/\gamma}$, *i.e.* taking the limit $\bar{\tau} \to 0$, our viscoelastic model reduces to the purely elastic model. In this limit, $\alpha = \sqrt{\bar{s}^2\Sigma + \bar{k}^2}$ and $\beta = \Sigma$ in the dispersion relation (eqn (20)). We examine how the instability depends on the dimensionless parameters Σ and $\bar{r}_0$.

4.1.1 Dependence on the rigid core radius and the elasto-capilliary number. We show the dispersion relation (eqn (20)) by plotting the dimensionless growth rate $\bar{s}$ as a function of the dimensionless wavenumber $\bar{k}$ for different values of Σ and a fixed $\bar{r}_0 = 0.1$ in Fig. 2(a). We see that for each curve, the unstable modes (*i.e.* $\bar{s} > 0$) lie within a certain range of dimensionless wavenumbers, *i.e.* $\bar{k}_1 < \bar{k} < \bar{k}_2$, where $\bar{k}_1$ and $\bar{k}_2$ are defined as $\bar{s}(\bar{k}_1) = 0$ and $\bar{s}(\bar{k}_2) = 0$. Within each range of unstable modes, there is a dimensionless wavenumber $\bar{k} = \bar{k}_m$ that corresponds to the fastest growing mode with a maximum dimensionless growth rate $\bar{s}_m \equiv \bar{s}(\bar{k} = \bar{k}_m)$. To study how the characteristic quantities depend on the control parameters, we plot $\bar{s}_m$, $\bar{k}_m$, and $\bar{k}_1$ (and $\bar{k}_2$) as a function of Σ respectively in Fig. 2(b)–(d) for three different dimensionless rigid core radii, *i.e.* $\bar{r}_0 = 10^{-9}$, $\bar{r}_0 = 0.1$ and 0.9. We also add the result of Tamim *et al.*[17] for the situation of a soft fibre without a rigid cylindrical core (*i.e.* $\bar{r}_0 = 0$). We see in Fig. 2(b) that for a fixed value of Σ, $\bar{s}_m$ is smaller for a larger $\bar{r}_0$. For all four different $\bar{r}_0$, the dimensionless growth rate of the fastest growing mode $\bar{s}_m$ decreases with decreasing Σ. When Σ is reduced to a critical value Σ_c, $\bar{s}_m$ drops to zero. There is no positive solution of $\bar{s}$ for $\Sigma < \Sigma_c$.

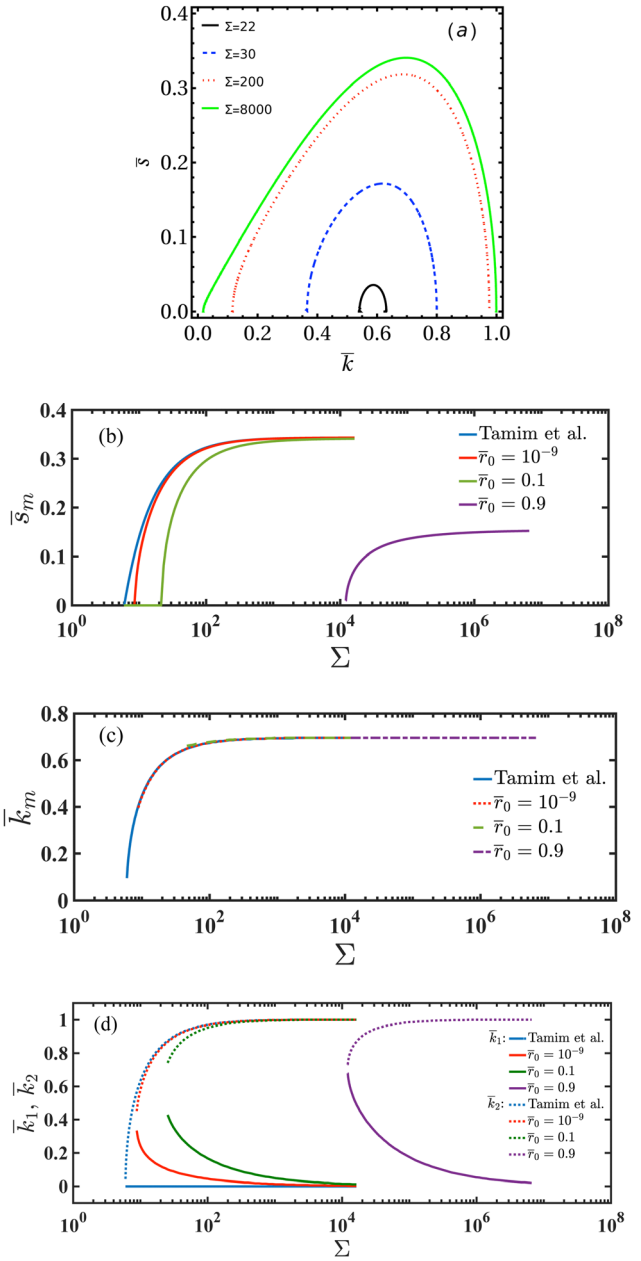

Fig. 2 (a) The dimensionless growth rate $\bar{s}$ as a function of the dimensionless wavenumber $\bar{k}$ for different values of Σ and a fixed $\bar{r}_0 = 0.1$ and $\bar{\tau} = 0$ (purely elastic). (b)–(d): The characteristic quantities $\bar{s}_m$ in (b), $\bar{k}_m$ in (c), and $\bar{k}_1$ and $\bar{k}_2$ in (d) as a function of Σ for four different dimensionless rigid core radius, *i.e.* $\bar{r}_0 = 0$ (from Tamim *et al.*[17]), $\bar{r}_0 = 10^{-9}$, $\bar{r}_0 = 0.1$ and 0.9. Other parameters: $\bar{\tau} = 0$.

This means that the coated elastic layer is stable under disturbance of any wavelength when $\Sigma < \Sigma_c$. We would also point out that, firstly, the critical value Σ_c for $\bar{r}_0 = 0.9$ is orders of magnitude larger than that for $\bar{r}_0 = 0.1$. This can be understood as follows: when the coated layer becomes thinner, the strain is larger and hence a softer layer can still generate strong enough elastic stress to resist the growth of disturbance. Secondly, even for the rigid cylindrical core radius as small as $\bar{r}_0 = 10^{-9}$, $\bar{s}_m$ starts to deviate significantly from that for the case of $\bar{r}_0 = 0$ when Σ is close to Σ_c. Moreover, the critical value Σ_c for $\bar{r}_0 = 10^{-9}$ ($\Sigma_c = 8.7$) is not the same as that for $\bar{r}_0 = 0$ ($\Sigma_c = 6$)[14,17] but larger. These features will be discussed in details in Section 4.1.2 where a stability phase diagram of Σ_c *vs.* $\bar{r}_0$ will be examined.

Interestingly, as shown in Fig. 2(c), we find that the dimensionless wavenumber of the fastest growing mode $\bar{k}_m$ is independent of the dimensionless radius of the rigid core $\bar{r}_0$, and decreases with reducing Σ. It is thus expected that elastic beads formed on a softer coated layer are closer together. When $\Sigma \to \infty$, we find $\bar{k}_m = 0.7$, which agrees with the dimensionless wavenumber of the fastest growing mode for the classical PRI of inviscid fluid threads.[10,11] Another remarkable point is that $\bar{k}_m$ starts to drop significantly with reducing Σ only when $\Sigma \lessapprox 10^2$. For cases with $\Sigma_c > 10^2$, *e.g.* for $\bar{r}_0 = 0.9$, the dimensionless wavenumber of the fastest growing mode is always close to the asymptotic value, *i.e.* $\bar{k}_m \approx 0.7$. Regarding the range of unstable modes, as we can see in Fig. 2(a) and (d), it shrinks when Σ is reduced. In contrast to the $\bar{r}_0 = 0$ case for which $\bar{k}_1$ remains zero, for non-zero $\bar{r}_0$ cases, $\bar{k}_1$ increases when Σ is reduced. This also means that the transition from unstable fibers to stable fibers (*i.e.* at $\Sigma = \Sigma_c$) occurs at $\bar{k}_m \neq 0$, which needs to be verified experimentally. It is expected that the bead separation formed on a soft fiber with a rigid core is finite ($\bar{k}_m \neq 0$) at the transition, instead of diverging for the $\bar{r}_0 = 0$ case.

4.1.2. Stability phase diagram. To show how the onset of instability depends on Σ and $\bar{r}_0$, we plot Σ_c (in log scales) as a function of $\bar{r}_0$ in a phase diagram, see Fig. 3(a). We see that increasing the radius of the rigid cylindrical core or decreasing the elastocapillary number can make the coated film more stable. Hence both the stiffness and the rigid core have a stabilizing effect. In Fig. 3(b), we plot Σ_c as a function of the thickness of the coated layer, *i.e.* $\bar{H} = 1 - \bar{r}_0$, in log–log scales. We find that when $\bar{r}_0 \gtrapprox 0.2$, the curve follows a power law $\Sigma_c = 21.5\,\bar{H}^{\lambda}$ where $\lambda \approx -2.75$. Hence the critical value Σ_c for a thin coated elastic film is orders of magnitudes larger than a thick

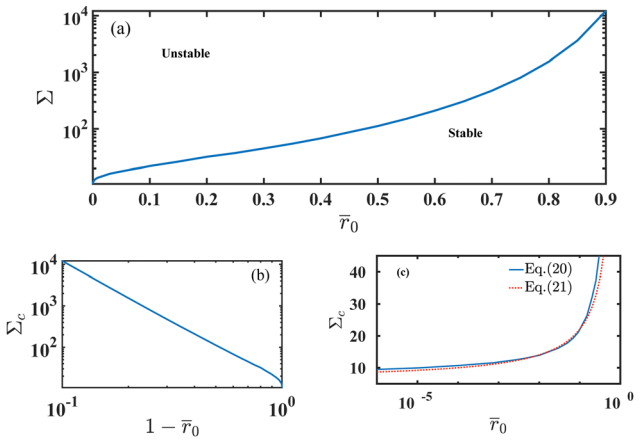

Fig. 3 (a) Stability phase diagram. Line: the critical elastocapillary number Σ_c (log scale) as a function of $\bar{r}_0$. (b) The critical elastocapillary number Σ_c as a function of $1 - \bar{r}_0$ in log–log scales. (c) A linear-log plot of the critical elastocapillary number Σ_c as a function of $\bar{r}_0$.

film. In the opposite limit of $\bar{r}_0 \to 0$, we find that our results can be approximately described by a logarithmic relation given as

$$\Sigma_c = \Sigma_{co} - \frac{a}{\log(\bar{r}_0)} \tag{21}$$

where $\Sigma_{co} = 6$ is the critical value for a soft elastic fibre without a rigid cylindrical core obtained by Mora *et al.*[14] or Tamim *et al.*,[17] and $a = 37$ is a fitting parameter. The comparison is shown in Fig. 3(c) for small $\bar{r}_0$. This result is consistent with the series expansion of the dispersion relation (eqn (20)) for small $\bar{r}_0$ given in Appendix 6.2.

4.2. Viscoelastic effects

We study the instability when $\bar{\tau} \neq 0$. We show results for two different rigid cylindrical core radii, namely $\bar{r}_0 = 0.1$ (a thick coated layer) and $\bar{r}_0 = 0.9$ (a thin coated layer). Since the critical elastocapillary numbers for $\bar{r}_0 = 0.1$ and $\bar{r}_0 = 0.9$ are different by orders of magnitude, we take a fixed value of $\Sigma = 50$ for the case of $\bar{r}_0 = 0.1$ and a fixed value of $\Sigma = 15\,000$ for the case of $\bar{r}_0 = 0.9$. In Fig. 4(a) and (b), we present the dispersion relation from eqn (20) for different $\bar{\tau}$, and in Fig. 4(c) and (d) for different n. We see that both $\bar{k}_1$ and $\bar{k}_2$ are independent of $\bar{\tau}$ and n. The dimensionless growth rate of the fastest growing mode $\bar{s}_m$ decreases when $\bar{\tau}$ is enhanced. This means that the viscoelastic relaxation of the material slows down the growth of disturbance. We also see that when $\bar{\tau}$ is increased, the dimensionless wavenumber of the fastest growing mode becomes smaller for $\bar{r}_0 = 0.1$ but remains constant for $\bar{r}_0 = 0.9$. When varying the other viscoelastic parameter n, the dimensionless growth rate of the fastest growing mode $\bar{s}_m$ decreases with decreasing $\bar{n}$. Hence smaller values of n have a larger damping effect. The change of $\bar{s}_m$ with varying $\bar{n}$ is more sensitive for $\bar{r}_0 = 0.9$ than for $\bar{r}_0 = 0.1$ as we can see in Fig. 4(c) and (d). The dimensionless wavenumber of the fastest growing mode $\bar{k}_m$ decreases slightly when n is increased from $n = 0.2$ to $n = 1$ for $\bar{r}_0 = 0.1$ but remains constant for $\bar{r}_0 = 0.9$.

Next, we take $\bar{\tau} = 100$ and $n = 0.5$, and show the results for $\bar{s}_m$ and $\bar{k}_m$ as a function of Σ for three different $\bar{r}_0 = 0$, 0.1 and 0.9 in Fig. 5. We see that the behaviors of $\bar{s}_m$ and $\bar{k}_m$ for $\bar{\tau} = 100$ are similar to those shown in Fig. 2(b) and (c) for the purely elastic case, *i.e.* $\bar{\tau} = 0$, except that when Σ is close to the critical value Σ_c. When Σ is approaching Σ_c, the curves for both $\bar{s}_m$ and $\bar{k}_m$ bend concavely, and the value of $\bar{k}_m$ becomes dependent on $\bar{r}_0$. However, varying the values of $\bar{\tau}$ or n does not change the critical values Σ_c, namely Σ_c remains the same as for the purely elastic case ($\bar{\tau} = 0$). When $\Sigma \to \infty$, viscoelastic effects disappear, and the results are the same as for the PRI of an inviscid fluid.[11]

It is also interesting to investigate the situation when keeping Σ finite, and taking the limit that the Deborah number $\bar{\tau} \to \infty$. It is then expected that viscoelastic effects dominate over inertial effects. We then introduce a dimensionless growth rate using the viscoelastic timescale τ (instead of the inertial-capillary time t_c) for the rescaling, *i.e.* $\bar{s}_\tau \equiv s\tau = \bar{s}\bar{\tau}$. The expression of β can be written as $\beta = \Sigma/(1 + \bar{s}_\tau^n)$. In the limit of $\bar{\tau} \to \infty$, $\bar{s} = \bar{s}_\tau/\bar{\tau} \to 0$, and thus $\alpha = \bar{k}$. Hence the dispersion relation (eqn (20)) consists of only the quantities $\bar{r}_0$, β and $\bar{k}$. Inertia plays no role in this limit. A plot of β *vs.* $\bar{k}$ from eqn (20) for $\bar{r}_0 = 0.1$ is shown in Fig. 6(a). The

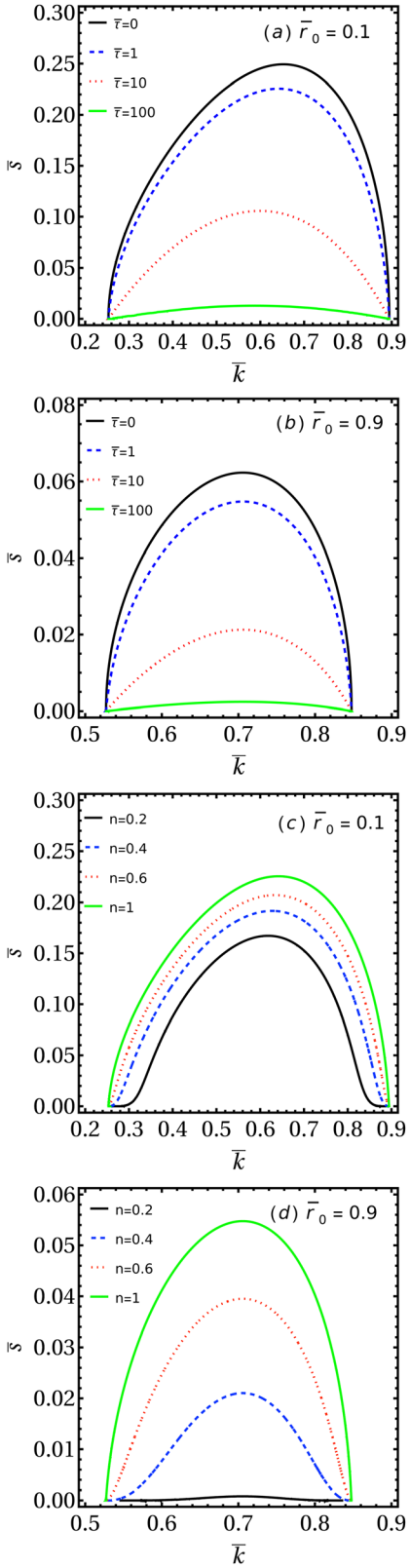

Fig. 4 The dimensionless growth rate $\bar{s}$ as a function of the dimensionless wavenumber $\bar{k}$ for different values of $\bar{\tau}$ and a fixed value of exponent $n = 1$ with $\bar{r}_0 = 0.1$ and $\Sigma = 50$ in (a), and $\bar{r}_0 = 0.9$ and $\Sigma = 15\,000$ in (b). The dimensionless growth rate $\bar{s}$ *vs.* the dimensionless wavenumber $\bar{k}$ for different values of exponent n and a fixed value of $\bar{\tau} = 1$ with $\bar{r}_0 = 0.1$ and $\Sigma = 50$ in (c), and $\bar{r}_0 = 0.9$ and $\Sigma = 15\,000$ in (d).

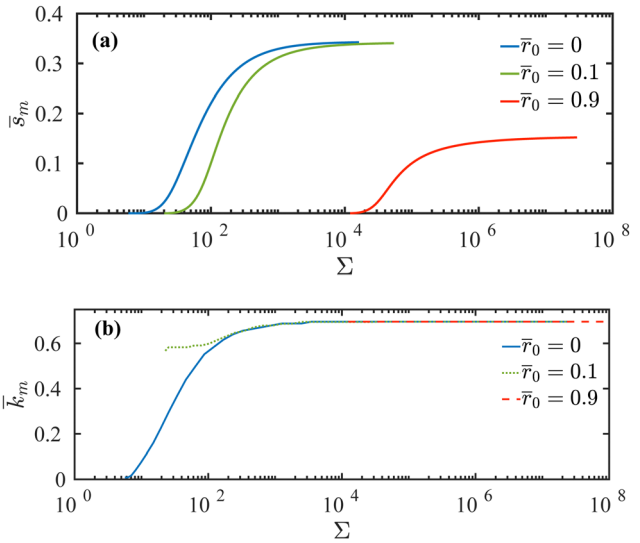

Fig. 5 The characteristic quantities $\bar{s}_m$ in (a) and $\bar{k}_m$ in (b) as a function of Σ for three different dimensionless rigid core radii, *i.e.* $\bar{r}_0 = 0$ (from Tamim *et al.*[17]), $\bar{r}_0 = 0.1$ and 0.9. Other parameters: $\bar{\tau} = 100$ and $n = 0.5$.

dimensionless maximum growth rate $\bar{s}_{\tau,m}(\bar{k}_m)$ can be computed from the value of β_m, defined as the minimum of β. Namely, $\bar{s}_{\tau,m} = [\Sigma/\beta_m - 1]^{1/n}$. We can then find the critical elastocapillary number by putting $\bar{s}_{\tau,m} = 0$, and thus obtain $\Sigma_c = \beta_m$. For $\bar{r}_0 = 0.1$, we find that $\Sigma_c = 21.7$ (see Fig. 6(a)), which is the same as for the purely elastic case.

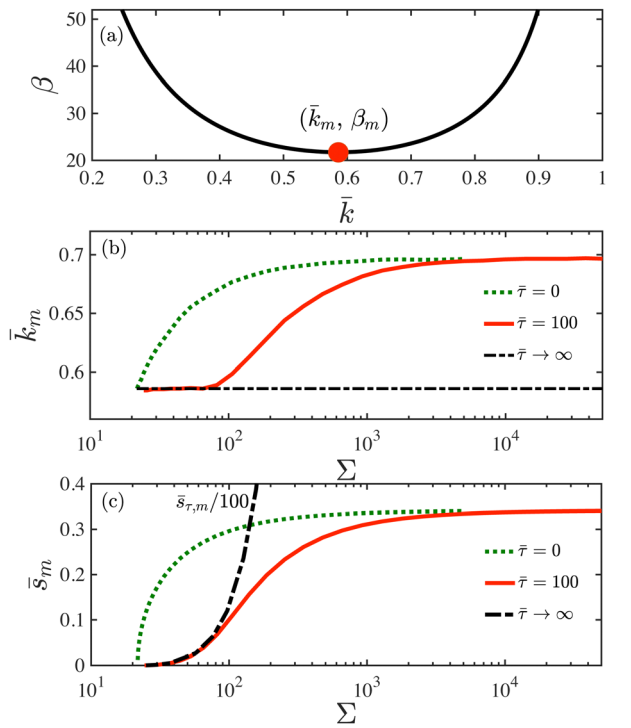

Fig. 6 (a) The relation between β and $\bar{k}$ for the limiting case of $\bar{\tau} \to \infty$. (b) and (c) The characteristic quantities $\bar{k}_m$ in (b) and $\bar{s}_m$ in (c) as a function of Σ for different values of $\bar{\tau}$. In (c) for $\bar{\tau} \to \infty$, the dashed-dotted curve represents $\bar{s}_{\tau,m}/100$ *vs.* Σ. Other parameters: $\bar{r}_0 = 0.1$ and $n = 0.5$.

Lastly, we compare the results when varying $\bar{\tau}$. In Fig. 6(b), we plot $\bar{k}_m$ *vs.* Σ for $\bar{\tau} = 0$, 100 and when $\bar{\tau} \to \infty$. We can see that the curve of $\bar{k}_m$ for $\bar{\tau} = 100$ becomes flat when Σ is approaching Σ_c, which collapses with the constant value $\bar{k}_m = 0.586$ for the case of $\bar{\tau} \to \infty$. In Fig. 6(c), we plot $\bar{s}_m$ *vs.* Σ for $\bar{\tau} = 0$ and 100. To compare the results of $\bar{\tau} = 100$ and the case of $\bar{\tau} \to \infty$, we divide $\bar{s}_{\tau,m}$ for the case of $\bar{\tau} \to \infty$ by the value $\bar{\tau} = 100$ since $\bar{s} = \bar{s}_\tau/\bar{\tau}$, and add a curve for $\bar{s}_{\tau,m}/100$ *vs.* Σ in Fig. 6(c). We can see that for Σ close to Σ_c, $\bar{s}_m$ for $\tau = 100$ and $\bar{s}_{\tau,m}/100$ collapse. Hence for $\bar{\tau} \neq 0$, when Σ is approaching Σ_c, $\bar{s}_m \ll 1$ and viscoelastic effects dominate over inertial effects.

5 Conclusions

We investigate the onset of the PRI of a soft layer coated on a rigid cylinder by analytically deriving the dispersion relation using the linear stability analysis. We implement the Chasset–Thirion model for the viscoelastic response of the soft layer. We find that the stiffness (characterized by $1/\Sigma$) and the rigid cylindrical core (characterized by $\bar{r}_0$) have a stabilizing effect. The dimensionless growth rate of the fastest growing mode $\bar{s}_m$ decreases with decreasing Σ or increasing $\bar{r}_0$. Importantly, there exists a critical elastocapillary number Σ_c for each $\bar{r}_0$ such that the coated layer is stable for any $\Sigma < \Sigma_c$. The critical value depends strongly on $\bar{r}_0$. For example, for $\bar{r}_0 = 0.9$, the soft layer becomes unstable only when the fibre is very soft, namely when $\Sigma \geq 12\,100$. While for a soft fibre without a rigid core ($\bar{r}_0 = 0$), the onset of instability occurs at $\Sigma \approx 6$, which is three to four orders of magnitudes smaller. This remarkable result would be interesting to be verified by performing experiments for different soft coatings on a fibre. Regarding the dimensionless wavenumber of the fastest growing mode $\bar{k}_m$, we find that $\bar{k}_m$ decreases with decreasing Σ. Interestingly, $\bar{k}_m$ is independent of $\bar{r}_0$ for the purely elastic case.

Regarding the roles of the viscoelastic parameters $\bar{\tau}$ and n, we find that increasing the relaxation timescale of viscoelastic material $\bar{\tau}$ or reducing the power n can slow down the growth of disturbance. Changing either $\bar{\tau}$ or n has no effect on the critical elastocapillary number. However, for $\bar{\tau} \neq 0$, the curves for both $\bar{s}_m$ *vs.* Σ and $\bar{k}_m$ *vs.* Σ bend concavely when Σ is approaching Σ_c, and viscoelastic effects become dominant over inertial effects. The value of $\bar{k}_m$ becomes dependent on $\bar{r}_0$ when Σ is around Σ_c. On the other hand, viscoelastic effects disappear in the limit of $\Sigma \to \infty$.

Our linear stability analysis predicts the threshold of instability[14] and the fastest growing modes. When the undulation of the interface grows, elastic stresses become larger and could stop the growth.[14,18] To study the evolution of the undulation and the equilibrium shape of the deformed soft layer, nonlinear elastic or viscoelastic models are required as large deformation is expected.[18]

6 Appendices

6.1 Expressions of the boundary conditions

Using the expressions of the general solutions (eqn (13)–(15)) for the boundary conditions (eqn (16)–(19)) yields the following set of linear equations for the unknowns A_m.

$$A_1\bar{k}I_1(\bar{r}_0\bar{k}) - A_2i\bar{k}I_1(\bar{r}_0\alpha) - A_3\bar{k}K_1(\bar{r}_0\bar{k}) - A_4i\bar{k}K_1(\bar{r}_0\alpha) = 0, \tag{22}$$

$$A_1(i\bar{k})I_0(\bar{r}_0\bar{k}) + A_2\alpha I_0(\bar{r}_0\alpha) + A_3(i\bar{k})K_0(\bar{r}_0\bar{k}) - A_4\alpha K_0(\bar{r}_0\alpha) = 0, \tag{23}$$

$$\begin{aligned} &A_1\left\{\frac{\alpha^2+\bar{k}^2}{2}I_0(\bar{k}) - \bar{k}I_1(\bar{k}) - \frac{\beta}{2}(1-\bar{k}^2)\bar{k}I_1(\bar{k})\right\} \\ &+ A_2\left\{-i\bar{k}[\alpha I_0(\alpha) - I_1(\alpha)] + \frac{\beta}{2}i\bar{k}(1-\bar{k}^2)I_1(\alpha)\right\} \\ &+ A_3\left\{\frac{\alpha^2+\bar{k}^2}{2}K_0(\bar{k}) + \bar{k}K_1(\bar{k}) + \frac{\beta}{2}(1-\bar{k}^2)\bar{k}K_1(\bar{k})\right\} \\ &+ A_4\left\{i\bar{k}[\alpha K_0(\alpha) + K_1(\alpha)] + \frac{\beta}{2}i\bar{k}(1-\bar{k}^2)K_1(\alpha)\right\} = 0, \end{aligned} \tag{24}$$

and

$$A_1 2i\bar{k}^2 I_1(\bar{k}) + A_2(\bar{k}^2+\alpha^2)I_1(\alpha) - A_3 2i\bar{k}^2 K_1(\bar{k}) + A_4(\bar{k}^2+\alpha^2)K_1(\alpha) = 0 \tag{25}$$

6.2 Dispersion relation for small core radii

We expand the determinant $D(\bar{k},\bar{s},\bar{r}_0,\bar{\tau},n)$ of the dispersion relation (eqn (20)) in series of $\bar{r}_0$ and the leading order terms are given as follows:

$$D(\bar{k},\bar{s};\bar{r}_0,\bar{k},\bar{\tau},n) = F_1 + F_2\ln(\bar{r}_0) + \ldots, \tag{26}$$

where

$$\begin{aligned} F_1 = {} & 2(C_2D_1 - C_1D_2)\gamma_E(\alpha-\bar{k})(\alpha+\bar{k}) - 2i\alpha^2(B_2D_1 - B_1D_2)\bar{k}K_0(\alpha) \\ & + i(B_2D_1 - B_1D_2)\bar{k}(\alpha^2+\bar{k}^2)K_0(\bar{k}) + \alpha[2\alpha^2(B_2C_1 - B_1C_2) \\ & - i(2+\beta)(B_2D_1 - B_1D_2)\bar{k} + 2(B_2C_1 - B_1C_2)\bar{k}^2 \\ & + i\beta(B_2D_1 - B_1D_2)\bar{k}^3]K_1(\alpha) + i\bar{k}^2[(2+\beta)(B_2D_1 - B_1D_2) \\ & + 4i(B_2C_1 - B_1C_2)\bar{k} + \beta(-B_2D_1 + B_1D_2)\bar{k}^2]K_1(\bar{k}), \end{aligned} \tag{27}$$

$$F_2 = 2\alpha^2\ln(\alpha/2)(C_2D_1 - C_1D_2) + 2(-C_2D_1 + C_1D_2)\bar{k}^2\ln(\bar{k}/2) \tag{28}$$

and

$$B_1 = (i\bar{k})I_0(\bar{r}_0\bar{k}),$$

$$B_2 = \alpha I_0(\bar{r}_0\alpha),$$

$$C_1 = \frac{\alpha^2+\bar{k}^2}{2}I_0(\bar{k}) - \bar{k}I_1(\bar{k}) - \frac{\beta}{2}(1-\bar{k}^2)\bar{k}I_1(\bar{k}),$$

$$C_2 = -i\bar{k}[\alpha I_0(\alpha) - I_1(\alpha)] + \frac{\beta}{2}i\bar{k}(1-\bar{k}^2)I_1(\alpha),$$

$$D_1 = 2i\bar{k}^2 I_1(\bar{k}),$$

$$D_2 = (\bar{k}^2+\alpha^2)I_1(\alpha),$$

γ_E is Euler's constant $\approx$ 0.57721.

6.3 Validation of our model: the Newtonian fluid limit

Our viscoelastic model reduces to the Newtonian fluid when $n = 1$ and in the limits of $\mu_o \to 0$ and $\mu_o\tau \to \eta$, where η is the dynamic viscosity of the fluid. In terms of the dimensionless parameters, it means $\Sigma \to \infty$ and $\Sigma/\tilde{\tau} \to \mathrm{Oh} \equiv \eta/\sqrt{\rho\gamma R}$, where Oh is called the Ohnesorge number. In this limiting situation, the dimensionless governing eqn (11) is reduced to

$$\hat{s}\frac{\partial^2\bar{u}_i}{\partial x_j\partial x_j} - \frac{\partial\bar{p}}{\partial x_i} = \frac{\hat{s}^2\bar{u}_i}{\mathrm{Oh}^2}, \tag{29}$$

where we have introduced a new rescaled growth rate $\hat{s} \equiv \eta Rs/\gamma = \mathrm{Oh}\bar{s}$. The dispersion relation is obtained by substituting

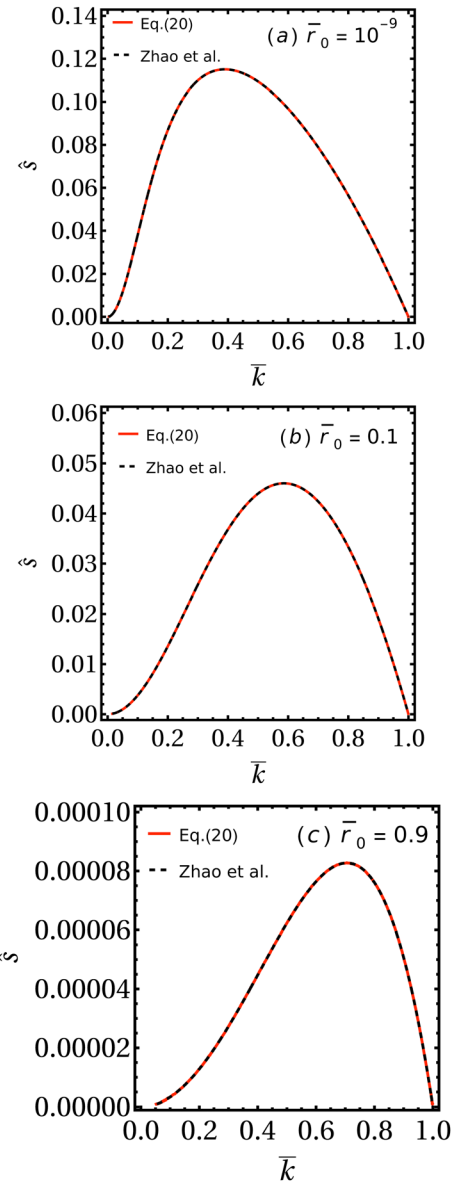

Fig. 7 The dispersion relation between the growth rate $\hat{s}$ and the wavenumber $\bar{k}$ in the Stokes flow limit for $\bar{r}_0 = 10^{-9}$ in (a), $\bar{r}_0 = 0.1$ in (b) and $\bar{r}_0 = 0.9$ in (c). Solid lines: our results when substituting $\alpha = \bar{k}$ and $\beta = 1/\hat{s}$ for eqn (20). Dashed lines: results of Zhao *et al.*[32]

$\alpha = \sqrt{\hat{s}/\mathrm{Oh}^2 + \hat{k}^2}$ and $\beta = 1/\hat{s}$ in eqn (20). The dimensionless control parameters are Oh and $\bar{r}_0$.

6.3.1 Stokes flow case. Taking further the limit that $\mathrm{Oh} \to \infty$, eqn (29) reduces to the Stokes equation in Laplace space. The remaining dimensionless control parameter is only $\bar{r}_0$. We validate the expression of our dispersion relation (eqn (20)) in this limiting case by comparing our results with that of Zhao *et al.*[32] in which the dispersion relation is obtained using the normal mode method to solve the Stokes equations. Fig. 7 shows the comparison for the cases of very small fibre radius ($\bar{r}_0 = 10^{-9}$), thick coated liquid film ($\bar{r}_0 = 0.1$) and thin coated liquid film ($\bar{r}_0 = 0.9$).

Data availability

Data for this article, including the codes used to compute the data shown in the figures, are available at **https://doi.org/10.11582/2024.00099**.

Conflicts of interest

There are no conflicts to declare.

Acknowledgements

The authors gratefully acknowledge financial support from the Research Council of Norway (Project No. 315110).

References

1 Y. Guo, J. Bae, Z. Fang, P. Li, F. Zhao and G. Yu, *Chem. Rev.*, 2020, **120**, 7642–7707.
2 Z. G. Qian, S. C. Huang and X. X. Xia, *Nat. Chem. Biol.*, 2022, **18**, 1330–1340.
3 I. Levental, P. C. Georges and P. A. Janmey, *Soft Matter*, 2007, **3**, 299–306.
4 B. Roman and J. Bico, *J. Phys.: Condens. Matter*, 2010, **22**, 493101.
5 A. Jagota, D. Paretkar and A. Ghatak, *Phys. Rev. E*, 2012, **85**, 051602.
6 M. L. Wei, *Europhys. Lett. (EPL)*, 2014, **106**, 14002.
7 R. W. Style, A. Jagota, C. Y. Hui and E. R. Dufresne, *Annual Rev. Cond. Matter Phys.*, 2017, **8**, 99–118.
8 J. Bico, É. Reyssat and B. Roman, *Annu. Rev. Fluid Mech.*, 2018, **50**, 629–659.
9 J. A. F. Plateau, *Acad. Sci. Bruxelles Mem.*, 1843, **16**, 3.
10 L. Rayleigh, *Proc. Roy. Soc. London*, 1879, **10**, 4.
11 J. Eggers and E. Villermaux, *Rep. Progr. Phys.*, 2008, **71**, 036601.
12 M. Taffetani and P. Ciarletta, *Phys. Rev. E*, 2015, **E91**, 032413.
13 C. Xuan and J. Biggins, *Phys. Rev. E*, 2017, **95**, 1–8.
14 S. Mora, T. Phou, J. M. Fromental, L. M. Pismen and Y. Pomeau, *Phys. Rev. Lett.*, 2010, **105**, 1–4.
15 C. Lestringant and B. Audoly, *Proc. R. Soc. A*, 2020, **476**, 20200337.
16 Y. Fu, L. Jin and A. Goriely, *J. Mech. Phys. Solids*, 2021, **147**, 104250.
17 S. I. Tamim and J. B. Bostwick, *Soft Matter*, 2021, **17**, 4170–4179.
18 A. Pandey, M. Kansal, M. A. Herrada, J. Eggers and J. H. Snoeijer, *Soft Matter*, 2021, **17**, 5148–5161.
19 B. Dortdivanlioglu and A. Javili, *Extreme Mech. Lett.*, 2022, **55**, 101797.
20 G. Yang, C. F. Gao and C. Q. Ru, *Int. J. Solids Struct.*, 2022, **241**, 111491.
21 C. Q. Ru, *Mech. Res. Communicat.*, 2022, **124**, 103959.
22 P. P. Bhat, S. Appathurai, M. T. Harris, M. Pasquali, G. H. McKinley and O. A. Basaran, *Nat. Phys.*, 2010, **6**, 625–631.
23 D. Quéré, *Annu. Rev. Fluid Mech.*, 1999, **31**, 347–384.
24 H.-C. Chang and E. A. Demekhin, *J. Fluid Mech.*, 1999, **380**, 233–255.
25 I. L. Kliakhandler, S. H. Davis and S. G. Bankoff, *J. Fluid Mech.*, 2001, **429**, 381–390.
26 C. Ruyer-quil, P. Treveleyan, F. Giorgiutti-dauphiné, C. Duprat and S. Kalliadasis, *J. Fluid Mech.*, 2008, **603**, 431–462.
27 Y. Zheng, H. Bai, Z. Huang, X. Tian, F.-Q. Nie, Y. Zhao, J. Zhai and L. Jiang, *Nature*, 2010, **463**, 640–643.
28 S. Haefner, M. Benzaquen, O. Bäumchen, T. Salez, R. Peters, J. D. McGraw, K. Jacobs, E. Raphaël and K. Dalnoki-Veress, *Nat. Commun.*, 2015, **6**, 7409.
29 A. Sadeghpour, Z. Zeng and Y. S. Ju, *Langmuir*, 2017, **33**, 6292–6299.
30 H. Chen, T. Ran, Y. Gan, J. Zhou, Y. Zhang, L. Zhang, D. Zhang and L. Jiang, *Nat. Mater.*, 2018, **17**, 935–942.
31 H. Ji, C. Falcon, A. Sadeghpour, Z. Zeng, Y. S. Ju and A. L. Bertozzi, *J. Fluid Mech.*, 2019, **865**, 303–327.
32 C. Zhao, Y. Zhang and T. Si, *J. Fluid Mech.*, 2023, **954**, 1–22.
33 S. L. Goren, *J. Fluid Mech.*, 1962, **12**, 309–319.
34 S. L. Goren, *J. Colloid Sci.*, 1964, **19**, 81–86.
35 Y. Zhang, S. T. Ellison, S. Duraivel, C. D. Morley, C. R. Taylor and T. E. Angelini, *Bioprinting*, 2021, **21**, e00121.
36 M. M. Fitzgerald, K. Bootsma, J. A. Berberich and J. L. Sparks, *Biomacromolecules*, 2015, **16**, 1497–1505.
37 D. K. Nandakumar, Y. Zhang, S. K. Ravi, N. Guo, C. Zhang and S. C. Tan, *Adv. Mater.*, 2019, **31**, 1806730.
38 R. Bar-Ziv and E. Moses, *Phys. Rev. Lett.*, 1994, **73**, 1392–1395.
39 E. Hannezo, J. Prost and J.-F. M. C. Joanny, *Phys. Rev. Lett.*, 2012, **109**, 018101.
40 D. Gonzalez-Rodriguez, S. Sart, A. Babataheri, D. Tareste, A. I. Barakat, C. Clanet and J. Husson, *Phys. Rev. Lett.*, 2015, **115**, 088102.
41 M. R. King and S. Petry, *Nat. Commun.*, 2020, **11**, 270.
42 S. U. Setru, B. Gouveia, R. Alfaro-Aco, J. W. Shaevitz, H. A. Stone and S. Petry, *Nat. Phys.*, 2021, **17**, 493–498.